# Journal of Geophysical Research: Solid Earth

# The crustal structure of the western Himalayas and Tibet

Amy Gilligan[1,2], Keith F. Priestley[1], Steven W. Roecker[3], Vadim Levin[4], and S. S. Rai[5]

[1]Bullard Laboratories, Department of Earth Sciences, University of Cambridge, Cambridge, UK, [2]Now at Department of Earth Science and Engineering, Imperial College London, London, UK, [3]Department of Earth and Environmental Sciences, Rensselaer Polytechnic Institute, Troy, New York, USA, [4]Department of Earth and Planetary Sciences, Rutgers, State University of New Jersey, New Brunswick, New Jersey, USA, [5]Indian Institute of Science Education and Research, Pune, India

**Abstract** We present new, high-resolution, shear velocity models for the western Himalayas and West Tibet from the joint inversion of *P* receiver functions recorded using seismic stations from four arrays in this region and fundamental mode Rayleigh wave group velocity maps from 5–70 s covering Central and Southern Asia. The Tibetan Plateau is a key locality in understanding large-scale continental dynamics. A large number of investigations has examined the structure and processes in eastern Tibet; however, western Tibet remains relatively understudied. Previous studies in this region indicate that the western part of the Tibetan Plateau is not a simple extension of the eastern part. The areas covered by these arrays include the Karakoram and Altan-Tagh faults, and major terrane boundaries in West Tibet and the Himalayas. The arrays used include broadband data collected by the West Tibet Array, a U.S.-China deployment on the western side of the Tibetan Plateau between 2007 and 2011. We use the shear wave velocity models to obtain estimates of Moho depth. The Moho is deep (68–84 km) throughout West Tibet. We do not observe significant steps within the Moho beneath West Tibet. A large step in Moho depth is observed at the Altyn-Tagh fault, where Moho depths are 20–30 km shallower to the north of the fault compared to those to the south. Beneath the Lhasa Terrane and Tethyan Himalayas, we observe a low-velocity zone in the midcrust. This feature is not interrupted by the Karakoram Fault, suggesting that the Karakoram Fault does not cut through the entire crust.

## 1. Introduction

The Tibetan Plateau, with an area of ~2.5 million km² and an average elevation of 4500 m, is the largest and highest plateau on Earth. A product of the ongoing collision between India and Eurasia, it is a key location for investigating contemporaneous continental geodynamics. Much has been learned over the past several decades about the central and eastern part of the plateau as a result of major projects such as INDEPTH [*Nelson et al.*, 1996; *Zhao and Nelson*, 1993; *Yuan et al.*, 1997; *Zhao et al.*, 2001, 2011], Hi-CLIMB [*Nábělek et al.*, 2009], and other deployments [e.g., *Acton et al.*, 2011; *Schulte-Pelkum et al.*, 2005] that provided images of the local seismic velocity structure.

Studies using receiver function and surface wave data [*Acton et al.*, 2011; *Nábělek et al.*, 2009; *Schulte-Pelkum et al.*, 2005; *Kind et al.*, 2002] find that the Moho is located at a depth of ~70–80 km beneath southeastern Tibet, shallowing to ~60–70 km below northeastern Tibet. Surface wave studies [*Rapine et al.*, 2003; *Cotte et al.*, 1999] and studies using the joint inversion of surface wave and receiver function data [*Bao et al.*, 2015] report a low velocity zone in the midcrust in southeastern Tibet. Similarly, magnetotelluric [e.g., *Wei et al.*, 2001] and seismic reflection [e.g., *Brown et al.*, 1996] studies observe what they interpret to be a hot, fluid-rich zone in the midcrust. While intriguing, the nature and extent of these low-velocity regions in midcrust remain contentious.

There is also a strong disagreement concerning the state of the lithosphere of Tibet, primarily because of uncertainty as to how far north Indian lithosphere currently extends beneath the plateau. Some [e.g., *Houseman et al.*, 1981; *Molnar et al.*, 1993] argue that low shear wave velocities observed in the upper mantle beneath northeast Tibet show that Indian lithosphere has delaminated beneath the northern part of the plateau. Alternatively, estimates of lithospheric thickness from more extensive surface wave observations [*Griot et al.*, 1998; *Priestley et al.*, 2006] suggest that a thick (~260 km) lithosphere exists throughout most, if not all, of Tibet. *McKenzie and Priestley* [2008] argue that a process of cratonization is going on beneath Tibet and that the low velocities in the upper mantle are the result of radiogenic heating of the crust.

Western Tibet is even less well understood than eastern Tibet, mostly because physical and political conditions make access difficult. While there are no major changes in surface features between the east and west of the plateau, western Tibet is somewhat higher (5000 m compared to 4500 m) and significantly narrower (400 km compared to 1000 km) than eastern Tibet. The small number of studies previously conducted in the region infer higher wave speeds in the upper mantle beneath western Tibet than eastern Tibet from Rayleigh wave group velocities [*Brandon and Romanowicz*, 1986], advances in S wave travel times from earthquakes in West Tibet [*Molnar*, 1990], and advances in the arrival times of SS phases with bounce points in West Tibet compared to those with bounce points beneath eastern Tibet [*Dricker and Roecker*, 2002]. This suggests that West Tibet might be at a different stage of development than East Tibet or that the geodynamic models for the east do not apply to the west.

The structure of the crust in West Tibet is largely unknown. Figure 1 shows the major faults and suture zones in West Tibet. *Wittlinger et al.* [2004] and *Zhao et al.* [2010] estimated crustal thickness along quasi-linear arrays from the Lhasa Terrane across West Tibet to the Tarim Basin at longitudes of $\sim 80°E$ and $\sim 82°E$, respectively, using a Common Conversion Point (CCP) stacking receiver function method. Both studies observe a significant shallowing (by $\sim$20 km) of Moho depth north of the Altyn Tagh Fault at the northern edge of Tibet. *Zhao et al.* [2010] infer that the Moho is at approximately 80 km depth beneath the plateau.

*Wittlinger et al.* [2004] suggest there is a 12 km step in the Moho at the Bangong-Nijiang Suture between the Lhasa (78 km) and Qiangtang Terranes (90 km). The Moho depth for the Qiangtang Terrane would be the deepest estimate of the Moho on Earth. *Rai et al.* [2006] jointly invert surface wave and receiver function data from a broadband deployment on the far western side of the plateau to infer a Moho depth of 75 km. A recent study by *Zhang et al.* [2014] uses H-$\kappa$ stacking to obtain estimate Moho depths of 67.5–88.5 km beneath the Lhasa and Qiangtang block along a transect running along 80°N. *Zhang et al.* [2014] also argue that their observation of a conversion from a layer $\sim$20 km shallow than the Moho suggests that the lower crust beneath part of the Lhasa Terrane has been eclogitized.

Several large strike-slip faults, such as the Altyn Tagh and the Kunlun Faults, cut the North Tibetan Plateau. West Tibet is dominated by the dextral Karakoram Fault, which initiated some 11–18 Ma [*Yin and Harrison*, 2000]. Some [*Leech*, 2008; *Klemperer et al.*, 2013; *Razi et al.*, 2014] suggest that the Karakoram Fault cuts completely through the crust and acts as a barrier to transport of material, while others are skeptical of this view [*Searle and Phillips*, 2008].

In this study we analyze recently recorded seismic data from western Tibet and northwest India to generate new images of seismic velocity structure of the crust. These images improve our understanding of the western part of the Indo-Eurasian collision zone and help to resolve questions of how crustal thickness varies across this region, the extent and nature of low-velocity zones in the midcrust and the role played by strike-slip faults.

## 2. Data

This study analyzes data from four seismic experiments in Northwest India and West Tibet: (1) the 2001 French deployment (YT), (2) the 2002–2003 Northwest India deployment (NG), (3) the 2005–2008 NGRI deployment (UT), and (4) the 2007–2011 US-China West Tibet array (Y2) (Figure 1).

The 2001 French experiment in West Tibet [*Wittlinger et al.*, 2004] consisted of short period and broadband stations recording at 54 sites, extending from near the southern edge of the Tarim Basin across the Kunlun Wedge, the Tianshuihai Terrane, the Qiangtang Terrane, ending in the Lhasa Terrane about 40 km north of the Karakoram Fault (Figure 1). The experiment lasted only 5 months, and only eight of the sites had true broadband sensors. These stations are referred to as the YT array in this paper.

The 2002–2003 Northwest India experiment [*Rai et al.*, 2006] consisted of 15 broadband seismometers deployed by the National Geophysical Research Institute (NGRI) along a $\sim$500km profile extending from the Indian Foreland Basin, across the Himalayan foothills, the Lesser Himalayas, the Greater Himalayas, the Tethyan Himalayas to the Karakoram Fault (Fig. 1). We also include data from two additional broadband stations operated by the University of Cambridge between 2002 and 2008. These 17 stations are referred to as the NG array in this paper.

Between 2005 and 2008, NGRI [*Mahesh et al.*, 2012, 2013; *Ashish et al.*, 2009] operated broadband seismometers at 37 sites in the Kumaon-Garawal Himalaya crossing the Main Frontal Thrust (MFT), Main
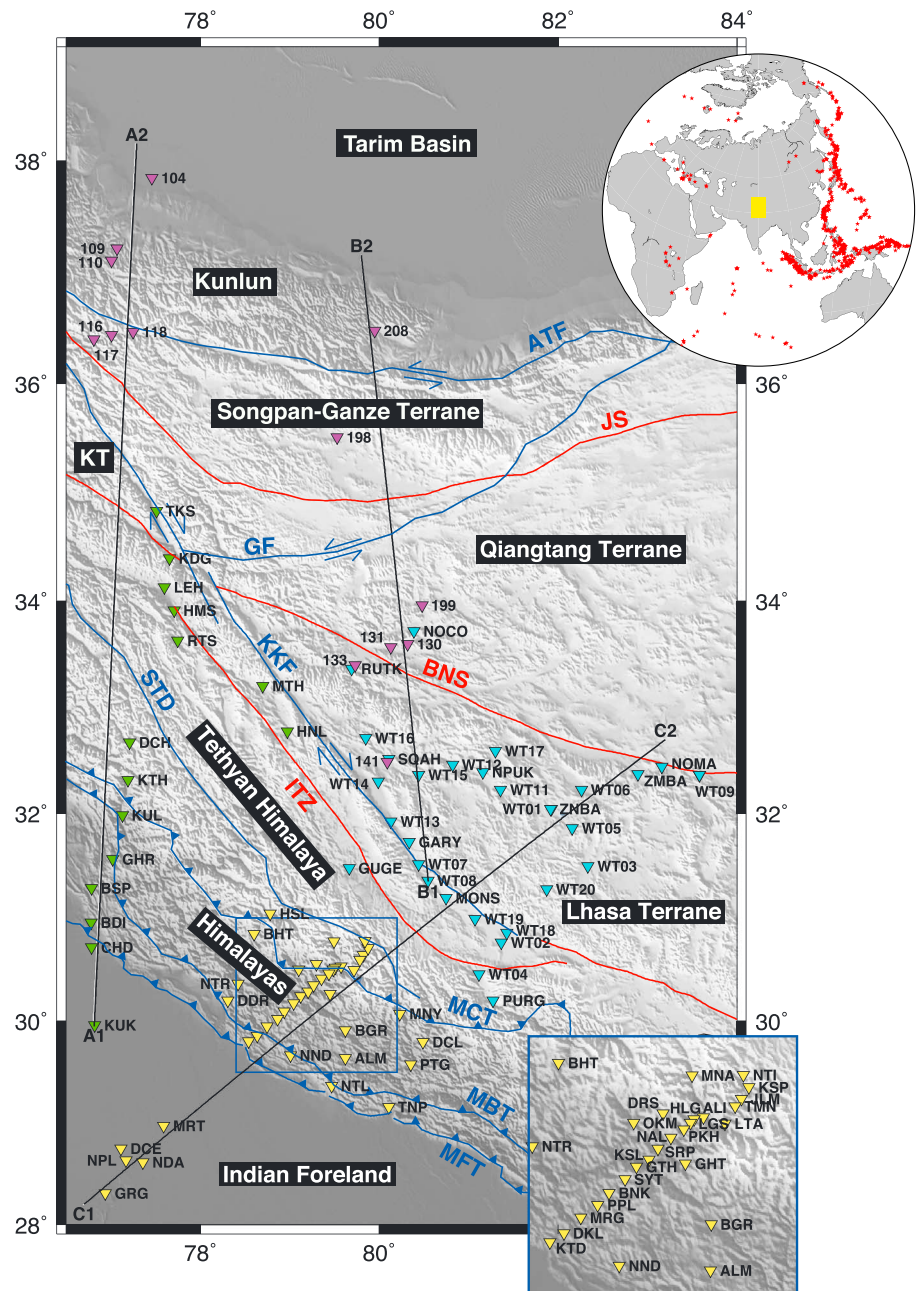
**Figure 1.** The region around the NG, UT, Y2 and YT arrays. Inverted triangles are stations: cyan, Y2; green, NG; and yellow, UT; magenta, YT. Red lines mark terrane boundaries: IZS, Indus-Zangbo Suture; BNS, Bangong-Nijiang Suture; JS, Jinsha Suture. Blue lines show the location of major faults: MFT, Main Frontal Thrust; MBT, Main Boundary Thrust; MCT, Main Central Thrust; KKF, Karakoram Fault; GF, Ghoza Fault; ATF, Altyn-Tagh Fault. KT marks the location of the Karakoram Terrane. The blue rectangle highlights the bottom inset region. (top inset) Red stars mark the locations of earthquakes used to construct the P receiver functions. The yellow box marks the location of the stations. The majority of events used were in the Pacific or Sumatra. Events were within the distance range 30–90°.

Boundary Thrust (MBT), and Main Central Thrust (MCT), ending just south of the South Tibetan Detachment (STD). These seismometers consisted of Guralp CMG-3T or Guralp CMG-3ESP sensors recording at 50 samples per second on 24-bit Reftex data loggers. Additional data came from a site operated by the University of Cambridge between 2002 and 2008. This site contained a Guralp CMG-3TD sensor and a Guralp DCM data logger, sampling at 100 samples per second. The NGRI deployment took place in two stages. Several of the sites remained installed for the 3 year duration of the experiment, but most of the sites were operated

for ~18 months then moved to new sites for a further 18 months. Twenty of the stations were installed along a profile with a station spacing of ~10 km, extending from the MFT to the STD. The remaining stations were dispersed about the profile (Figure 1). These stations are referred to as the UT array.

The 2007–2011 U.S.-China West Tibet array was deployed in the western part of the Tibetan Plateau (Figure 1) with a station spacing is approximately 40–100 km. The array consisted of 30 Streckeisen STS-2 seismometers, recorded by Quanterra Q330 acquisition systems sampling at 100 sps. Deployment was in two phases: 10 stations operated for the entire period (2007–2011), and a further 20 were installed in 2009 and operated until mid-2011. The array covered an area that includes the Karakorum fault and Indus-Zangbo and Bangong-Nijiang sutures. These stations are referred to as the Y2 array.

## 3. Methodology

To determine a crustal model we analyze teleseismic receiver functions computed from seismograms recorded on the arrays described above. Further, we obtain fundamental mode surface wave group velocities measured from regional distance earthquakes recorded on the Y2 array and other stations throughout Tibet, India, Pakistan, and elsewhere in central Asia and from ambient noise analysis using data from the Y2 array. Receiver functions are sensitive to short wavelength velocity changes (e.g., the Moho) but with a strong velocity depth trade-off. The velocity depth trade-off has been extensively examined by *Ammon et al.* [1990]. *Ozalaybey et al.* [1997] suggested jointly inverting receiver functions with surface wave dispersion data to reduce the nonuniqueness of receiver functions. The dispersion data constrain the crustal thickness and absolute crustal shear wave speed about the site, and the receiver function superimposes short wavelength details. This is especially important in the Himalaya where *P* receiver functions can be complex.

### 3.1. Receiver Functions

Seismograms from earthquakes between 30° and 90° epicentral distance, greater than magnitude 4.5, were used to calculate radial and tangential *P* receiver functions. Because of the distance range and the location of the seismometers, the majority of the earthquakes that produce suitable seismograms are to the east of the stations, coming from the western Pacific and Indonesia. Receiver functions were computed only for events where the signal-to-noise ratio of the *P* arrival was high.

We calculated 12430 receiver functions using the time domain iterative deconvolution method of *Ligorria and Ammon* [1999]. A total of 2853 receiver functions (23%), for which the fit between the receiver function estimate convolved with the observed vertical component and radial component was less than 70%, were discarded. The remaining 9577 receiver functions were visually inspected. Any receiver functions that appeared noisy, oscillatory, or anomalous to other receiver functions from a similar distance and azimuth, were discarded, including all receiver functions from OKM in the UT array and WT16 in the Y2 array. This left 8242 individual receiver functions from 738 events (Figure 1) to be used in the analysis.

Stacking receiver functions is important to reduce noise. For the YT, Y2, UT, and NG arrays, all the individual receiver functions for each station were stacked into a single stack for that station. The structure beneath a station can vary with azimuth. Figures 2d and 3d show examples of the azimuthal variations that are observed in receiver functions from the same station. Therefore, individual receiver functions for stations in the Y2, UT, and NG rays were stacked in narrow (< 30°) azimuthal bins at each station. There are many more events to the east of the stations than to the west (Figure 1), which means that, in many cases, stacks for eastern azimuths include many more receiver functions than are stacked for western azimuths. The stations in the YT array were operational for a much shorter period of time (5 months), and consequently, it was not possible to calculate as many receiver functions for stations in this array. Therefore, receiver functions for these stations could not be stacked in narrow azimuthal bins.

### 3.2. Ambient Noise Analysis

Surface waves dispersion curves extracted from intrastation Green's functions from ambient noise cross correlations allow for a greater range of paths to be sampled, giving a larger number of crossing paths in a surface wave tomographic model. Furthermore, ambient noise studies usually provide short-period group velocity measurements that cannot be obtained from earthquake data. Using surface waves extracted from ambient noise can, therefore, help improve the resolution of tomographic models.

We follow the method of *Bensen et al.* [2007] to obtain intrastation Green's functions from ambient noise data for the Y2 array. We use continuous recordings of the vertical component of motion between station pairs
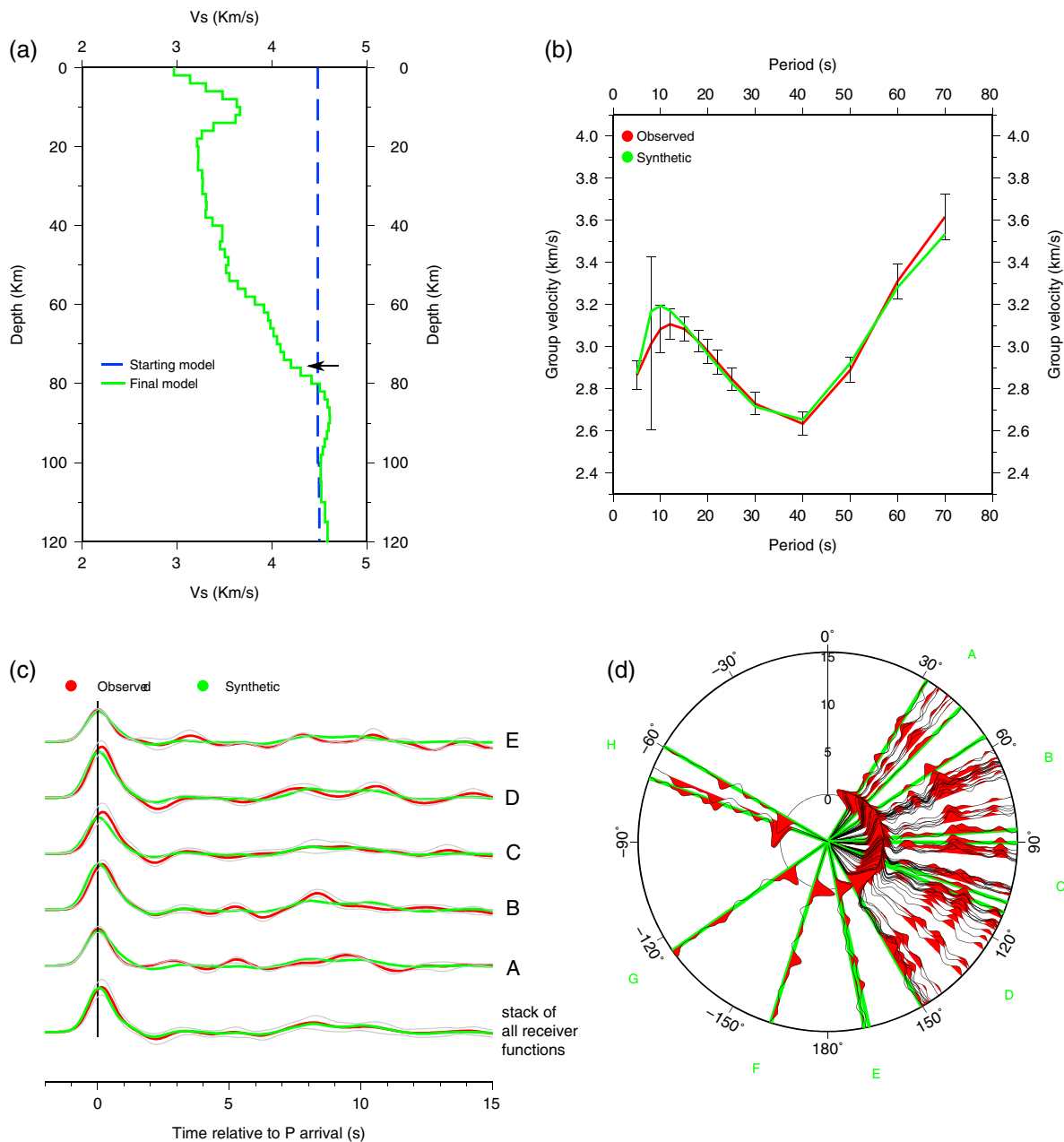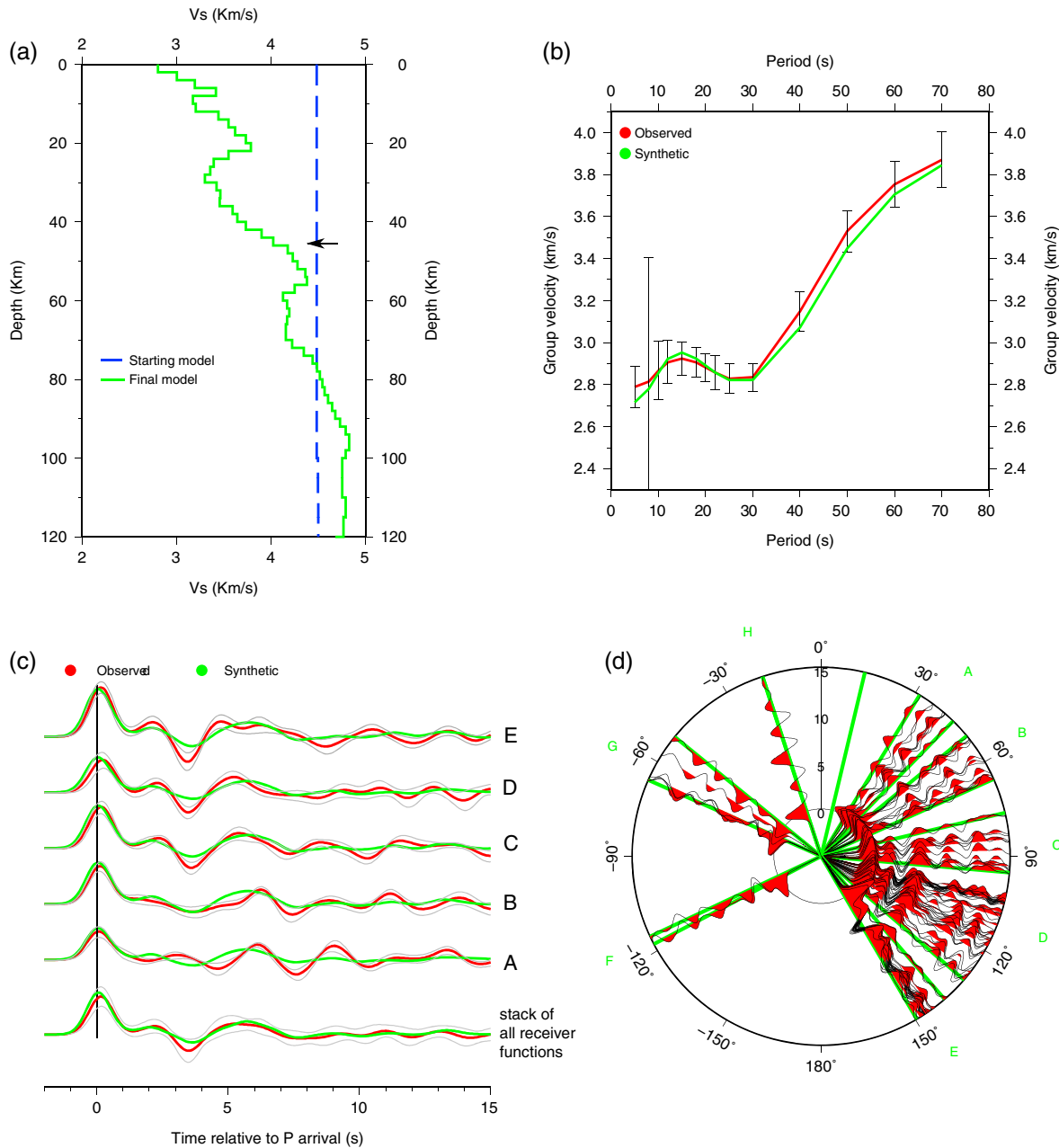
**Figure 2.** Joint inversion results for the station WT12. (a) Shear velocity models: the dashed blue line is the starting model and the green line is the final model after the joint inversion using a *p* value of 0.05. (b) Data (red) and synthetic group velocity curve for WT12. The green curve is the dispersion curve which results from the final model after the joint inversion using a *p* value of 0.05. (c) Stacked receiver function observations (red) and synthetic receiver functions (green) for the final model from the joint inversion. (d) The individual receiver functions used in the stacks. The green lines mark the bounds of each stack. Positive signals are filled in red on the receiver functions plotted in Figure 2d.

where the seismograms are decimated to 1 sps, split into 1 day intervals, band-pass filtered from 0.01 to 0.2 Hz, spectrally whitened, and normalized using a running mean normalization to remove signals from earthquakes prior to cross correlation. The time series for each day and for each station pair are cross-correlated, and the resultant cross correlations for each station pair are stacked. A total of 368 stacked cross correlations were produced. We take an average of the causal and acausal sides of the cross correlation as the Green's function. Multiple filter analysis with phase-matched filtering [*Herrmann and Ammon*, 2004] was used to

**Figure 3.** Individual and stacked *P* receiver functions and joint inversion results for the station DCL. Results are plotted as described in Figure 2. A *p* value of 0.05 is used in the inversion.

extract dispersion curves from the cross correlations. Fundamental mode Rayleigh wave group velocity dispersion curves were calculated for 143 paths.

The ambient noise group velocity measurements for the Y2 array are added to the larger data set of Rayleigh wave dispersion measurements from earthquakes throughout central Asia. The inclusion of ambient noise data from the Y2 array means that in the vicinity of this array there is a high path density down to short periods (to 5 s), meaning there is the potential for high-resolution group velocity maps to be constructed for this area.

### 3.3. Fundamental Mode Rayleigh Wave Group Velocities
The fundamental mode Rayleigh wave data set has group velocity measurements from 5–70 s from a total 15448 paths throughout central Asia obtained using multiple filter analysis with phase-matched filtering

[*Herrmann and Ammon*, 2004]. The entire area is parameterized by a 2-D mesh of triangular elements. A node spacing of 1° is used throughout the majority of the area; however, in the vicinity of the Y2 region, at short periods (5–15 s), the node spacing used is finer because of the particularly high path density in this region. The group slowness at each node is calculated from intersecting paths following *Mitra et al.* [2006]. An a priori constraint is placed on the standard deviation of the slowness across a reference distance to stabilize the inversion. Maps for 5 s to 70 s are obtained. Pseudo-dispersion curves were extracted from the group velocity maps for the locations of stations in the YT, NG, UT, and Y2 arrays for a priori slowness values between 0.03 and 0.08 using bicubic interpolation. A further 120 pseudo-dispersion curves are extracted for points at 1° spacings from 76–85°E, 28–39°N.

### 3.4. Joint Inversion

Pseudo-dispersion curves and radial *P* receiver function stacks for each station are inverted for shear velocity structure using *joint96* [*Herrmann and Ammon*, 2004]. In cases where there are less than three receiver functions in a stack, or where the standard deviation is of a similar magnitude to the signal in the receiver function, the stacks have not been included in the inversion. This removed 342 receiver functions from the analysis or 4% of the total. The inversion procedure is nonlinear and therefore may be influenced by the starting model used in the inversions. We test several starting models: starting models with velocities of 4.48 km/s, which is the mantle velocity in the ak135 model [*Kennett et al.*, 1995], 4.28 km/s and 4.68 km/s and $V_p/V_s$ values of 1.79 down to 100 km, parameterized into 2 km thick layers, overlying ak135. Since these models do not include any preconceived ideas about the crustal thickness, any of the crustal structure in the inversion is dictated by the data. We discuss the models resulting from a starting model of velocities of 4.48 km/s in the crust. Perturbing the starting model by ±0.2 km/s does not alter the resulting crustal structure. In a few cases where a station was situated on thick sediment, a shear wave speed of 4.48 km/s was too high for the inversion to converge. In these cases we compute synthetic receiver functions and group velocity dispersion curves using a model which includes a thin, low-velocity layer in the uppermost crust.

One of the subjective parameters of the joint inversion is the relative weighting between the receiver functions and the surface wave dispersion measurements. We tested *p* values of 0.5, 0.1, 0.05, 0.001, and 0.0001, where the larger the number, the greater the contribution from surface waves. Inversions are allowed to run until the misfit reduction is 0.005%, meaning the number of iterations in the inversion is not the same for each station. A preferred model for each station is chosen that maximizes the weight of the receiver function data, while maintaining a good fit to the surface wave data. Checkerboard tests (A. Gilligan and K. F. Priestley, manuscript in preparation, 2015) show that the smallest features we are able to resolve in the surface group velocity maps in this region are ~1°. Receiver functions have a somewhat better lateral resolution. We therefore want to maximize the weight of the receiver functions in joint inversions.

Finally, we inverted 120 group velocity measurements using *surf96* extracted at 1° spacings for the region 76–85°E, 28–39°N. We used a 4.48 km/s starting model, as in the joint inversions, parameterized in the same way as the starting model used in the joint receiver function and surface wave inversions. These inversions ran for 10 iterations, which was sufficient for the inversion to converge and to result in a good fit to the group velocity dispersion data.

## 4. Results

### 4.1. Stacked Receiver Functions

All the receiver functions for each station are combined in a single stack. Those lying within 75 km of line A1-A2 (Figure 1) are plotted in Figure 4a, those lying within 75 km of the line B1-B2 are plotted in Figure 4b, and those lying within 75 km of the line C1-C2 are plotted in Figure 4c. Positive signals (red) indicate a velocity increase with depth, while negative signals (unfilled) indicate a velocity decrease with depth. As is discussed in *Gilligan et al.* [2014], it is important to take into account the effect of the interference between conversions and multiples: a consequence is that the largest signal on a receiver function should not necessarily be interpreted as being due to the velocity increase at the Moho.

Beneath the Himalayan Foreland Basin (GRG-MRT) in line C1-C2 (Figure 4c), there is a strong signal at ~4 s. The first positive signal in the receiver function for MRT is delayed from 0 s, suggesting a conversion from the base of the sedimentary layer. The receiver functions for stations in the Himalayas along the section C1-C2 are complicated, with most having several peaks. There is a strong positive arrival around ~5–6 s in nearly all of the stacks, and one at ~3 s in some of the receiver functions. The peak at the longer delay time is likely to be
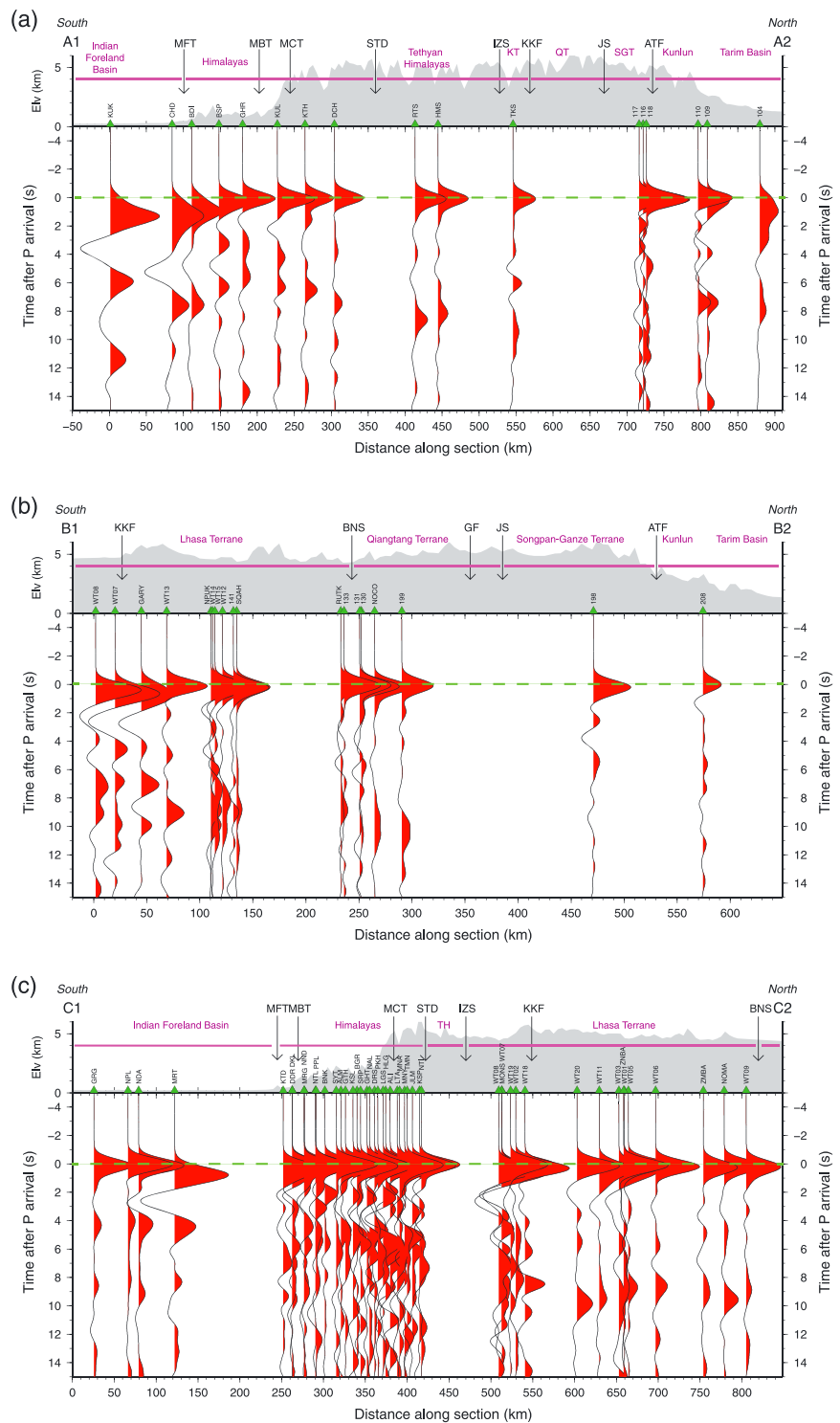
**Figure 4.** (a) Stacked *P* receiver functions along the line A1-A2 (29.95°N, 76.82°E–38.15°N, 77.29°E). (b) Stacked *P* receiver functions along the line B1-B2 (31.34°N, 80.55°E–37.16°N, 79.80°E). (c) Stacked *P* receiver functions along the line C1-C2 (28.2°N, 76.7°E–32.7°N, 83.2°E). In each case the stacked receiver functions for stations within 75 km of the line of section are projected onto the profile. The green dashed line marks the *P* arrival time. Positive arrivals, filled red, are indicative of a velocity increase with depth. Topography is plotted above. The location of stations along the line of section are shown as green triangles, and the locations of stations and major faults are marked. MFT, Main Frontal Thrust; MBT, Main Boundary Thrust; MCT, Main Central Thrust; STD, South Tibetan Detachment; ITZ, Indus-Zangbo Suture; KKF, Karakoram Fault; BNS, Bangong-Nijiang Suture; GF, Ghoza Fault; JS, Jinsha Suture; ATF, Altyn-Tagh Fault; TH, Tethyan Himalayas; QT, Qiangtang Terrane; SGT, Songpang Ganze Terrane.

from the Moho conversion, while the peak at the shorter delay time may possibly be the conversion from the Main Himalayan Detachment. For the stations in the Himalayas along line A1-A2 (Figure 4a), a coherent arrival can be traced from GHR to DCH between 5 s and 7 s. Delay times increase northward. For the two stations in the Tethyan Himalayas along section A1-A2, there is an arrival at ~8 s.

Across the Indus-Zangbo Suture, along line A1-A2, the receiver function for TKS shows two prominent arrivals, one at 6 s and a broader one at ~9.5 s. Using previous estimates of crustal thickness in West Tibet [*Zhang et al.*, 2014; *Wittlinger et al.*, 2004] as a guide, the arrival at 9.5 s is likely to be from the Moho. Along section C1-C2, the receiver functions between the Indus-Zangbo Suture and the Karakoram Fault are quite variable, and all have several large, positive arrivals. North of the Karakoram Fault, there is a large, consistent, positive arrival at 8.5–9.5 s. In some of the receiver functions there is also a small positive arrival at ~5 s. Stations along B1-B2 north of the Karakoram Fault also contain arrivals between 8.5–9.5 s.

For stations along line B1-B2 (Figure 4b) in Qiangtang Terrane a broad peak centered around 10 s delay time is observed. No such peak is observed for station 198 farther to the north in the Songpan-Ganze Terrane. Stations 116–118, lying along line A1-A2 are also in the Songpan-Ganze Terrane. Receiver functions for these stations have several positive arrivals. Arrivals at around 10 s are seen on receiver functions for all of these stations. For stations north of the Altyn Tagh Fault along A1-A2, the largest positive arrival occurs at 7–8 s. Stations 109 and 110 also contain a small positive arrival at 4 s, while station 104 has a first arrival delayed from 0 s, suggesting a strong arrival from the base of the sedimentary layer in the Tarim basin. Along line B1-B2, the stations north of the Altyn-Tagh Fault also contain arrivals at around 7 s, but also contain several other smaller arrivals at shorter and longer delay times.

### 4.2. Shear Wave Velocity Structure

A shear wave velocity model beneath each station was obtained by jointly inverting the receiver function stacks for the station and the fundamental mode Rayleigh wave dispersion curves extracted from the group velocity maps.

A 2-D velocity cross section is constructed along the line C1-C2 (Figure 5) by combining 1-D velocity models. The section extends from the Indian Foreland Basin into West Tibet, just north of the Bangong-Nijang Suture. In the midcrust, between 20 and 40 km, a low-velocity layer is observed in this cross section, throughout Tibet and south of the Karakoram Fault, into the Thethyan Himalayas. It does not appear to be interrupted by the Karakoram Fault or the Indus-Zangbo Suture. In the Lhasa Terrane, north of the Karakoram Fault, shear velocities are relatively high (average 3.45 km/s) before decreasing between 12 and 24 km. Velocities are then relatively low (average 3.13 km/s) to a depth of 34–46 km, where they increase once again.

We used a bootstrapping method to estimate the error in shear velocity. We take a random selection with replacement of individual receiver functions, equal to the total number of receiver functions for a station, and stack them. The stacked receiver function is then jointly inverted with the group velocity dispersion curve for that station to obtain a shear velocity model. This is done 500 times for each station. The resulting velocity models (Figure S1 in the supporting information) estimate the error in the velocity model to be less than 0.05 km/s and show that the joint inversion method is stable. This estimate of error is significantly less than the average change in velocity observed for the low-velocity layer (0.32 km/s), suggesting that this is a reliable feature.

In order to further refine the velocity models and test the robustness of the models, we test the features of the inversion models with forward modeling. The low velocities observed in the upper crust to midcrust have potentially important implications for the deformation processes occurring in this region. It is therefore necessary to ensure they are robust features, required by the data.

We compute synthetic receiver functions and dispersion curves from models that do not contain these velocity variations and compare these to the observed data. Forward modeling demonstrates that this low-velocity layer, seen between distances 470 km and 800 km in Figure 5 at a depth of ~20–40 km, and the relatively high-velocity layer above it, are robust features. The low-velocity layer is required to fit the low group velocities in the Rayleigh wave dispersion curves observed between 20 and 40 s at many sites. The high-velocity layer is necessary to fit the relatively high group velocities observed between 8 and 18 s. For NPUK (Figure 6), for example, it can be seen that if there is a gradual increase in velocity from 4 to 44 km, rather than the large velocity increase to 8 km, a decrease below this and then increasing velocity from around 38 km, the synthetic
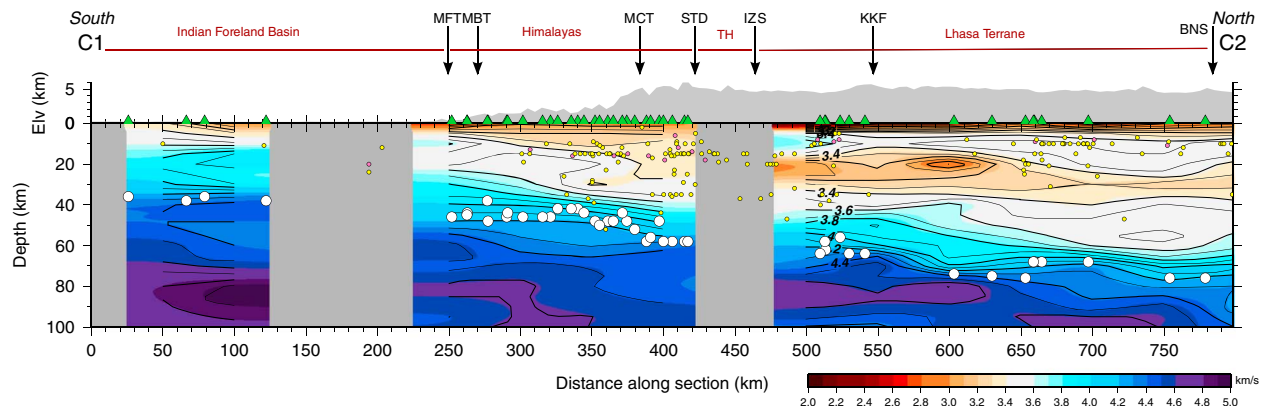
**Figure 5.** Shear wave velocity versus depth along the line C1-C2 (28.2°N, 76.7°E–32.7°N, 83.2°E) from the joint inversion of *P* receiver functions and fundamental mode Rayleigh wave data. Pink circles are earthquake locations from Sloan et al. (2011), yellow circles are earthquake locations from Engdhal (2009). The white circles are Moho depths estimated from the shear velocity models for each station. The green triangles show the locations of stations. MFT, Main Frontal Thrust; MBT, Main Boundary Thrust; MCT, Main Central Thrust; STD, South Tibetan Detachment; ITZ, Indus-Zangbo Suture; KKF, Karakoram Fault; BNS, Bangong-Nijiang Suture; TH, Tethyan Himalayas. Grey regions on the cross section are where there are gaps in station coverage. The green triangles are stations, as in Figure 4c.

group velocity dispersion curve does not fit the observed group velocity dispersion. The high velocities in the upper crust are necessary to fit the high group velocities between 8 and 25 s.

The peak seen in radial *P* receiver function at 0 s is due to the direct *P* arrival; however, if there is a strong conversion at the basement interface with the sediments, this conversion can interfere with the direct *P* arrival, resulting in an apparent delayed first arrival. For some stations, the synthetics produced from the model resulting from the joint inversion fails to fit the arrival around the 0 s time. The fit, in many cases, can be improved by decreasing the velocity in the upper few kilometers of the crust. This shifts the first signal in the synthetics to a time shortly after the *P* arrival time. NPUK (Figure 6) is one example where the inclusion of a low-velocity layer in the uppermost crust improves the fit to the receiver functions.

Some of the receiver functions for stations in the Indian Foreland Basin (CHD, KUK, MRT, and DCE) and station 104 in the Tarim Basin are dominated by conversions from the sediment-basement interface. The velocity models from these stations are difficult to interpret, and the deeper portions are geologically unrealistic. No attempt is made to interpret the model resulting from the joint inversion at DCE. The joint inversions for the other stations where the receiver functions are dominated by a sedimentary signal are weighted to include a larger contribution from surface waves ($p = 0.5$) than is the case for most of the rest of the locations ($p = 0.1$–$0.01$).

For some stations, clear azimuthal variations are observed in the receiver functions. For WT12 (Figure 2), the receiver functions in stack A have a broad conversion around 9.5 s. In stack B there is a clearer, larger amplitude arrival at 8.5 s, stack C has a broad low-amplitude arrival between 8 and 10 s, and in stacks D and E a "double" arrival, with two prominent peaks at 7.5 and 10.5 s. In stacks D and E the signal at 10.5 s has a slightly larger amplitude. The velocity model has two relatively sharp velocity increases in the lower crust: one at 56 km and another at 80 km. Forward modeling demonstrates that the conversion at 10.5 s in stack A is best fit with a Moho at 73 km, while the conversion at 8.5 km in stack B is best fit with a Moho at 62 km. In the stacks with a double arrival, velocity increases at 56 km and 80 km are best able to reproduce the signal in the receiver function (Figure 7).

### 4.3. Moho Depth

One of the key questions we seek to address is how the Moho depth varies in West Tibet. Moho depths determined using the shear velocity models resulting from the joint inversion of group velocity and *P* receiver function data are summarized in Table S1 (supporting information). Additional Moho depths are estimated from the results of inverting group velocity data alone for shear velocity structure. Estimates of Moho depths are picked where the gradient of increasing shear velocity is steepest and where velocities exceed 4 km/s, ensuring these depths are consistent with the delay times of conversions in the receiver functions. Because of this, the velocity at the depth that is chosen for the Moho is not necessarily the same for each location. It is important to note that, in the velocity models in this study, the transition from the crust to the mantle occurs over a depth range: the Moho is gradational rather than being a sharp transition. Although we select one

NPUK
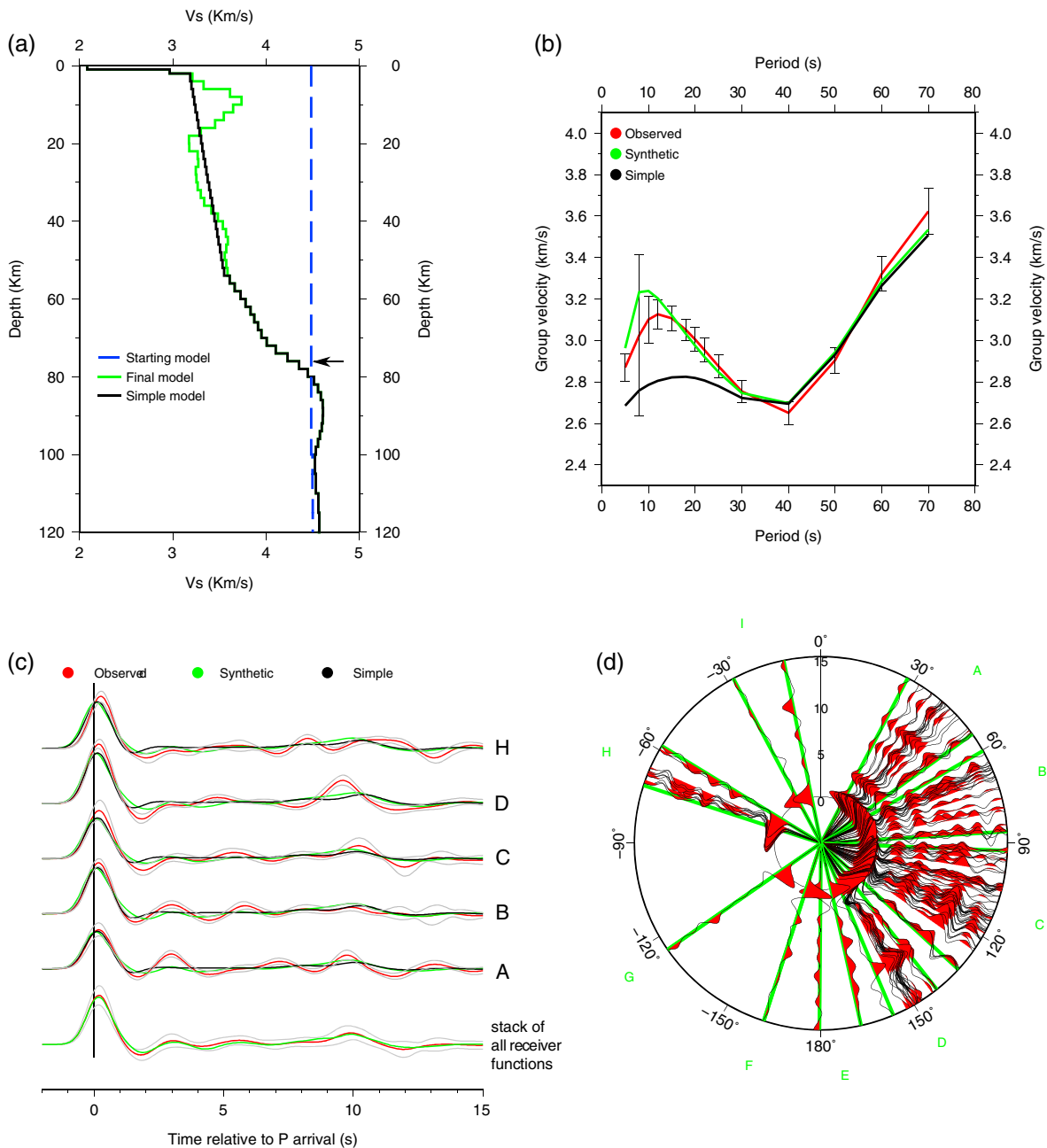


**Figure 6.** Individual and stacked *P* receiver functions and joint inversion results for the station NPUK. Results are plotted as described in Figure 2. A *p* value of 0.1 is used in the inversion. Results are plotted as described in Figure 2. The black line in Figure 6a is the a velocity model where the high and low velocities seen in the final model from the joint inversion have been replaced by a gradient between 6 and 56 km, and a low-velocity layer is included in the upper 1 km of the crust. The synthetic dispersion curve and receiver functions from this model are shown in Figures 6b and 6c as black lines.

depth as the Moho, other depths within this range could, arguably, be selected. We are consistent between models as to where we identify the Moho; therefore, we consider that the relative changes in Moho depth can be interpreted.

Using all of the Moho estimates, we show how the Moho depth varies across the region (Figure 8). In the Indian Foreland Basin, Moho depths are estimated to be 36–38 km. Moho depths increase northeastward up to the Altyn-Tagh Fault, with a strike roughly parallel to the strike of the front of the Himalayas and major faults in
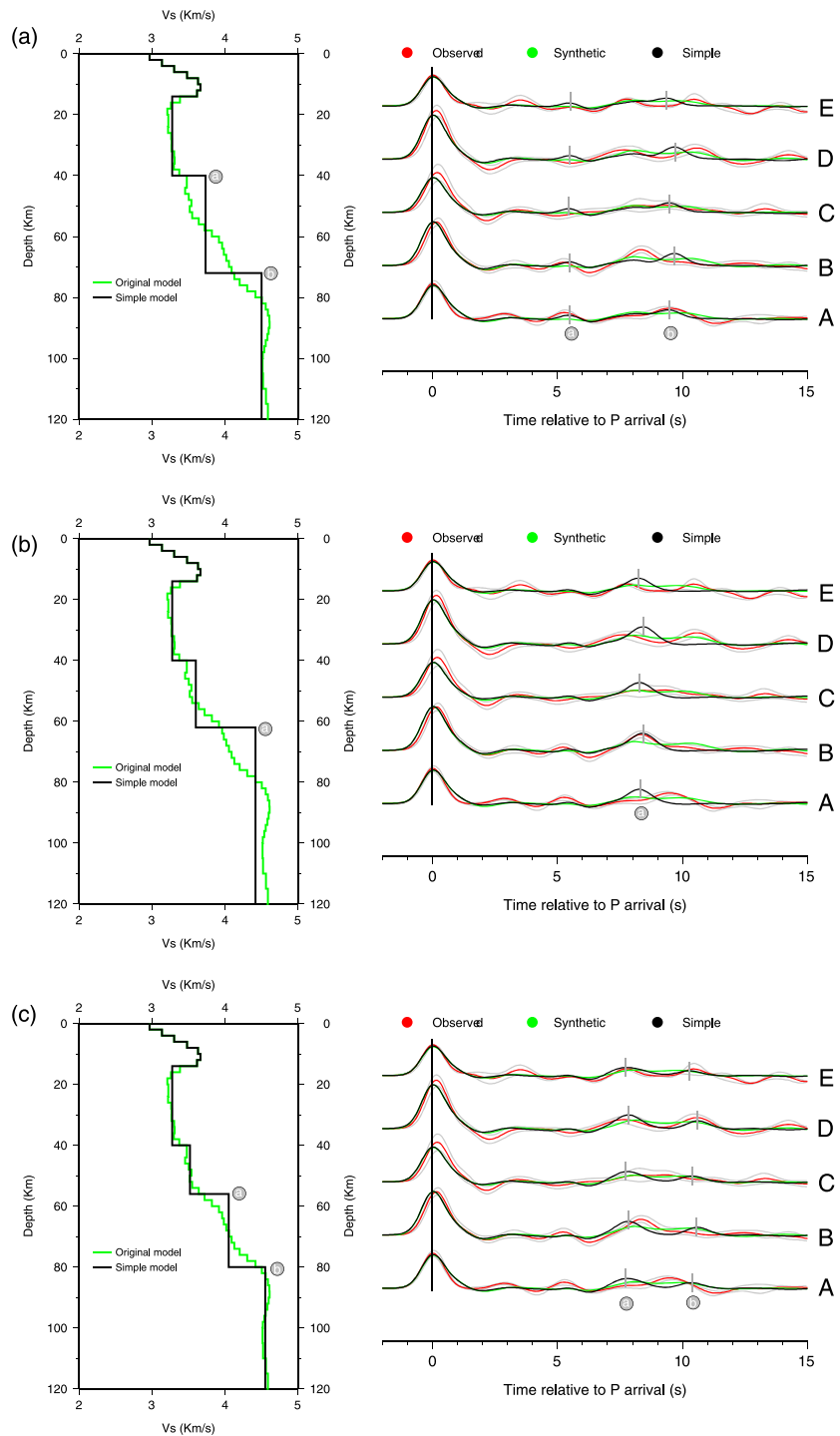
**Figure 7.** Forward modeling to test the location of velocity contrasts needed to reproduce signals seen in the stacked receiver functions at WT12. The plots on the left are the velocity models. The green line is the final model resulting from the joint inversion of receiver function and surface wave data, and the black line is the model being tested. The plots to the right are the stacked receiver functions, binned as shown in Figure 2. The red lines are the original data, the green lines are the synthetic receiver functions resulting from the model from the joint inversion, and the black line is the receiver function that results from the model that is being tested. (a) A model, and corresponding receiver functions, with a large velocity change at 73 km. This model is best able to reproduce the large signal seen at 10.5 s in stack A. (b) A model, and corresponding receiver functions, with a large velocity change at 62 km. This model is best able to reproduce the large signal seen at 8.5 s in stack B. (c) A model, and corresponding receiver functions, with two velocity changes of a similar magnitude at 56 km and 80 km. This model is best able to reproduce the signals seen at 7.5 and 10.5 s in stacks D and E.
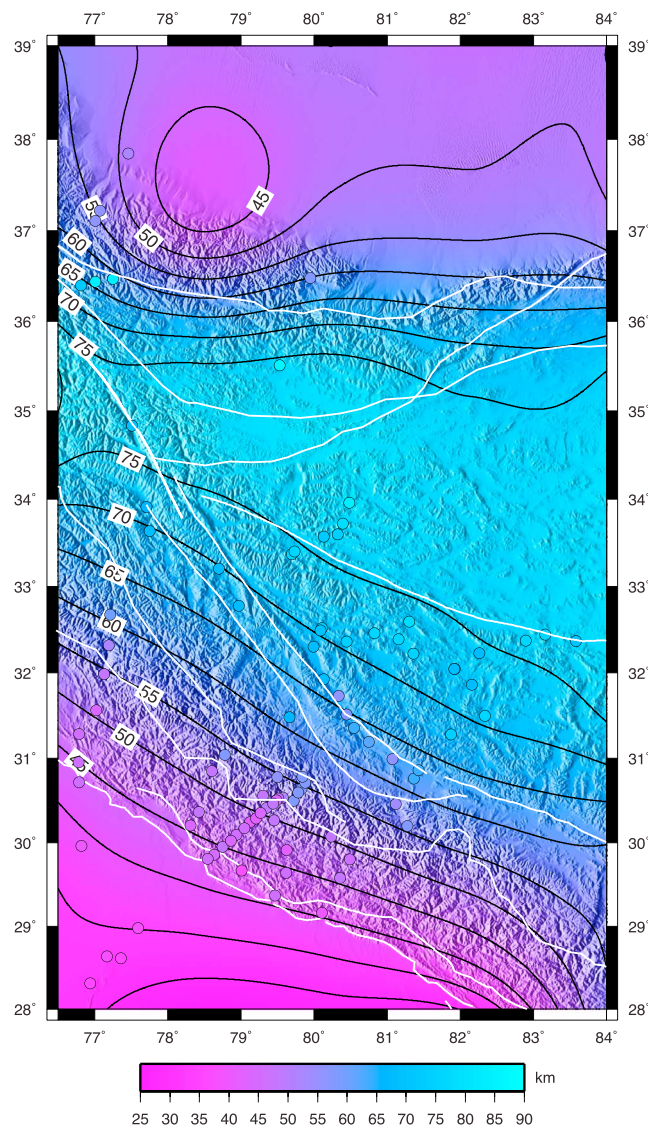
**Figure 8.** Contour plot of Moho depth variation in West Tibet determined using Moho depths estimated from the shear velocity structures resulting from the joint inversion of receiver function and surface wave data at stations shown in Figure 1, and the inversion of just surface wave data at points with 1° spacings from 76–85°E, 28–39°N. Circles are at the location of the stations in this study and are colored according to the Moho depth picked from the joint inversion of receiver function and surface wave data. The scale is the same for both the contour plot and circles. White lines are the major faults and suture lines, as shown in Figure 1.

the region. From the contours of Moho depth, which include estimates from both joint inversions and surface wave inversions which include just group velocity data, the gradient of increasing Moho depth is reasonably constant from the front of the Himalayas to the Karakoram fault, where the gradient shallows. Beneath most of the Lhasa, Qiangtang, and Songpan-Ganze Terranes there does not appear to be any large steps in Moho depth.

Across the Altyn Tagh Fault there is a shallowing of the Moho of ~20–30 km. Moho depths are greater than 80 km to the south of the ATF, whereas they are at ~56 km just north of the ATF. This difference in Moho depth can clearly be seen between stations 116 (south of the ATF) and 110 (north of the ATF) (Figure 9).

In general, the estimates of Moho depths made from the joint inversions at the location of stations agree well with Moho contour plot (Figure 8). The main differences are the estimates for stations in the Himalayas north of the Main Central Thrust, which are approximately 5 km deeper than suggested from the contour plot. A step in Moho depth of the order 10 km at the Main Central Thrust is clearly seen in the Moho depths estimated from shear velocity models (Figure 5). For stations south of the Altyn-Tagh Fault, Moho depths are significantly deeper (~15 km) than shown in the contour plots. While the resolution of the group velocities in this region is good, it does not have sufficient lateral resolution to distinguish a sharp change in Moho depth at the

Main Central Thrust or Altyn-Tagh fault. This highlights the value of jointly inverting receiver function and surface wave data.

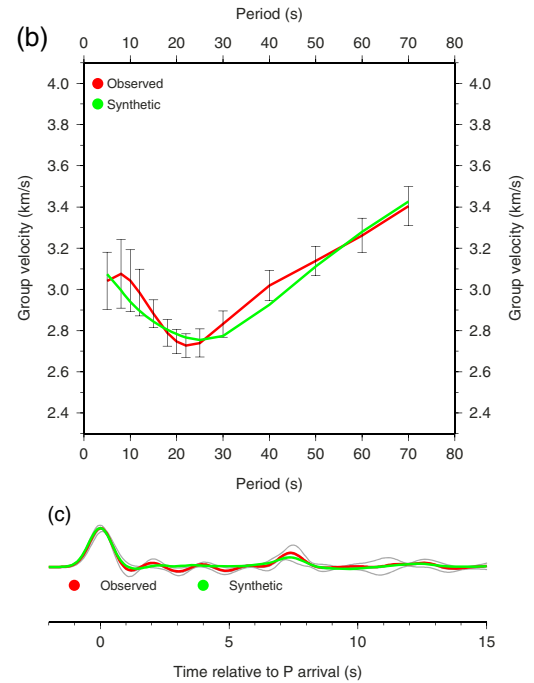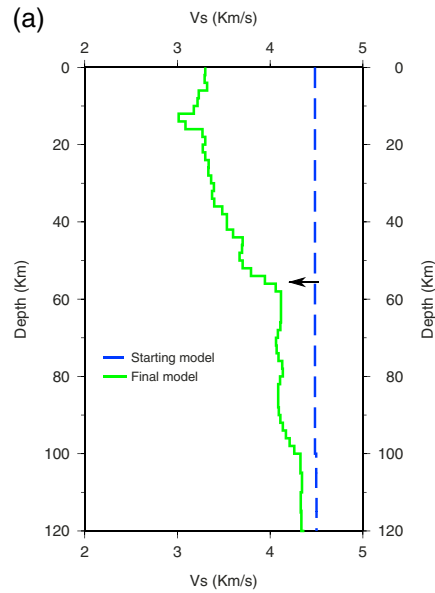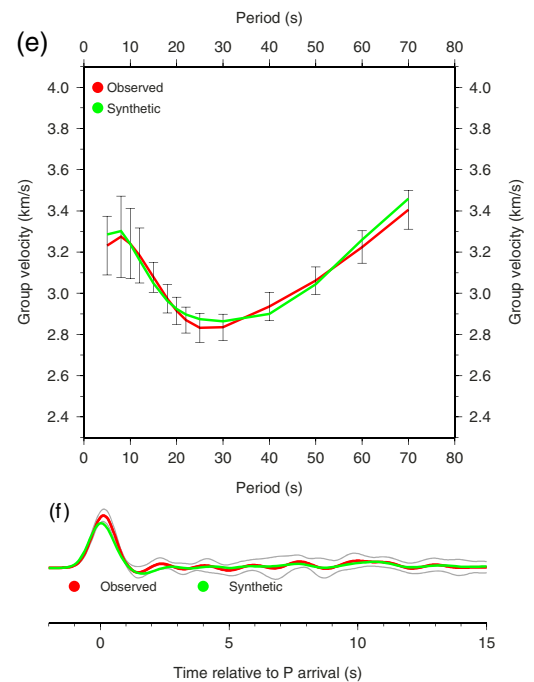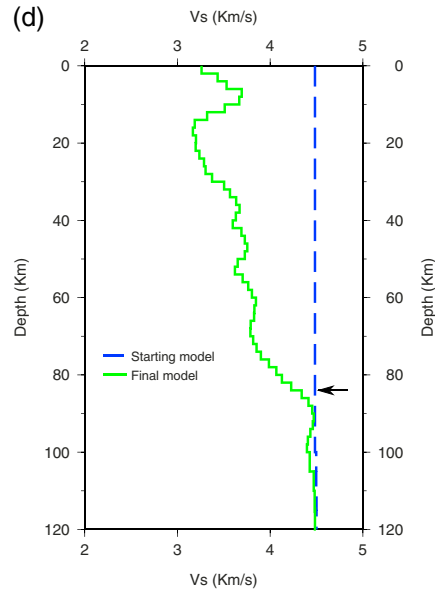## 5. Discussion

### 5.1. Moho Depth

Beneath the Himalayas, Moho depths for stations in the NG array are 5–10 km shallower than those estimated by *Rai et al.* [2006], who apply a joint inversion method identical to that used in this study to data from the NG array. The Moho depths observed by *Rai et al.* [2006] are deeper than those observed farther east in the Himalayas and southern Tibet [*Acton et al.*, 2011; *Caldwell et al.*, 2013; *Nábělek et al.*, 2009; *Schulte-Pelkum et al.*, 2005]. The Moho depths estimated for the NG array in our study show better agreement with results of studies

**Figure 9.** Shear velocity models for stations (a) 110 and (d) 116 showing the contrast in Moho depth between these two stations. (b and e) The group velocity dispersion curve data and synthetics for stations 110 and 116, respectively, and (c and f) the receiver function stack used in the inversion and resulting synthetic for each station.

to the east and are similar to those we estimate for stations in the UT array. There is a degree of subjectivity in where the Moho is picked in shear velocity models, which may account for some of the differences between the *Rai et al.* [2006] results and ours. Furthermore, the group velocity measurements used by *Rai et al.* [2006] are from *Mitra et al.* [2006]. These group velocity measurements have since been improved upon by A. Gilligan and K. F. Priestley (manuscript in preparation, 2015).

*Caldwell et al.* [2013] make Moho depth estimates from a CCP stack using data from some of the stations in the UT array. Their results appear to show that the Moho is slightly shallower in this part of the Himalayas than has been observed by other studies to the east [*Acton et al.*, 2011; *Nábělek et al.*, 2009; *Schulte-Pelkum et al.*, 2005] and west [*Rai et al.*, 2006]. Their Moho depths are also slightly shallower (∼5 km) than the Moho depth estimates from joint inversion in this study. The difference in Moho depth between those obtained using a CCP stacking method and joint inversion results are likely due to the shortcomings of the CCP method.

*Razi et al.* [2014] observe a change in body wave velocities at a depth of 70–80 km in their travel time tomography study using data from the Y2 array. They interpret this velocity change as being the Moho, the depth of which is in reasonable agreement with the depth of the Moho estimated from the shear velocity models in this study.

*Wittlinger et al.* [2004] calculate radial *P* receiver functions and Common Conversion Point (CCP) stacks for the stations in the YT array. There is good agreement with our study in northern Tibet: there is a large offset in Moho depth at the Altyn Tagh Fault, and Moho depths immediately south of the ATF are at approximately 84 km. *Zhao et al.* [2010] also image a Moho step of a similar magnitude in their CCP section along approximately 82°N. The Moho depths we observe just to the north of the ATF are shallower than the depth of 65 km observed by *Wittlinger et al.* [2004]. This may be because *Wittlinger et al.* [2004] use all of the stations in the YT array, including all of the short-period stations. We found that the receiver functions from stations in the YT were of lower quality than those for the other arrays. Therefore, we use receiver functions from only 13 of the YT stations, meaning we do not have results for stations as close to the ATF as *Wittlinger et al.* [2004] are.

*Wittlinger et al.* [2004] claim that the Moho is up to 90 km deep beneath the Qiangtang Terrane and suggest the Moho has a ∼12 km offset at the Bangong-Nijiang Suture (BNS). The Moho depths in our study agree with their estimates for Moho depth beneath the Lhasa Terrane (70–78 km in *Wittlinger et al.* [2004], 68–78 km in our study). The Moho depth (78 km) estimated for NOCO in the Qiangtang Terrane is significantly shallower than that observed by *Wittlinger et al.* [2004], and our estimates for Moho depth for the station 199 in the Y2 network is also shallower at 84 km. We do not see a step in the Moho as *Wittlinger et al.* [2004] do but instead observe the Moho gradually increasing in depth northward. The gradient of the increase shallows significantly once into the Lhasa and Qiangtang Terranes.

Our Moho depth estimates also agree well in the Lhasa Terrane with those of *Zhang et al.* [2014] (67.5–77 km in their study). Their Moho depths in the Qiangtang Terrane, obtained from H-$\kappa$ stacking of *P* receiver functions, (71.5–79 km) are within the range of those we obtain from joint inversion of receiver functions and surface waves (72–84 km). Unlike *Wittlinger et al.* [2004] who propose a Moho step at the BNS, *Zhang et al.* [2014] suggest that a more significant step in the Moho occurs at the fault we call the Ghoza Fault. We do not observe a step in the Moho at either of these locations. Consequently, we do not agree with the interpretation of *Zhang et al.* [2014] that small (<5 km) changes in Moho depth in the Lhasa Terrane is evidence of shearing along subvertical fault zones.

Depth migration, as used by *Wittlinger et al.* [2004] and *Zhang et al.* [2014], depends on the velocity model used in the CCP stack. In particular, there is a velocity depth trade-off in receiver functions, whereby the conversion from the base of a thin, low wave speed layer could produce a signal at the same time as the conversion from the base of a thick, high wave speed layer. Thus, the depths of impedance contrasts estimated from CCP stacks may be incorrect. *Schulte-Pelkum and Ben-Zion* [2012] demonstrate that failure to take different velocity structures across continental strike-slip faults results in apparent vertical Moho offsets when no such offset is present in the model. It may be that the differences in Moho depth in the Qiangtang Terrane between this study and *Wittlinger et al.* [2004] arise, in part, because of a uniform velocity used by *Wittlinger et al.* [2004] in performing the CCP stack.

Although there are some differences in the detail of Moho depths from between this study and previous work, the overall picture of Moho depths increasing to the north, a significant jump at the Main Central Thrust, depths remaining deep throughout Tibet, and a large step in the Moho at the Altyn Tagh fault are consistent. The continuity of the Moho observed in this study suggests that Tibet is likely to be underlain by Indian crust and upper mantle as far north as the Altyn-Tagh Fault.

The Moho in western Tibet appears to be gradational. This is observed in the shear velocity models resulting from joint inversion and is suggested by the relatively low amplitude and broad *P*-to-*S* phases, likely to be

from the Moho, in the *P* receiver functions. A gradational Moho potentially supports the interpretation of *Zhang et al.* [2014] that partial eclogitization has occurred in the lower crust. The gradational nature of the Moho cautions against the use of the H-$\kappa$ stacking technique in this region, as this can struggle to provide meaningful results where the Moho is gradational.

### 5.2. Midcrustal Low-Velocity Zone

*Caldwell et al.* [2009] observe a low-velocity zone similar to that observed in the midcrust beneath stations in Tibet in this study. Their group velocity study uses data from stations north of the South Tibetan Detachment in the NG array. *Rai et al.* [2006] do not observe a low- or high-velocity layer in the midcrust. While *Rai et al.* [2006] use the same method as in this study, their group velocity dispersion measurements only extend to 15 s whereas the dispersion measurements used in our study extend to 5 s. Thus, *Rai et al.* [2006] do not observe the high group velocities we observe between 8 and 18 s. They do observe lower group velocities between 20 and 40 s, but the decrease is not as significant as those observed in group velocity dispersion data used in this study.

*Oreshin et al.* [2008] also do not observe a low-velocity zone in the midcrust, apart from beneath MTH and HNL, in their velocity models obtained from the joint inversion of *P* and *S* receiver functions and travel time residuals. The low-velocity zone is a feature that is particularly required in the group velocity data, which may explain why it is not seen in the *Oreshin et al.* [2008] study. It should be noted, however, that the inclusion of a low-velocity zone does not worsen the fit to the receiver function data in our study. This highlights that jointly inverting receiver function and surface wave data can help to illuminate features in the Earth that an individual data type may not be sensitive to.

A low-velocity layer in the midcrust has also been observed [*Rapine et al.*, 2003; *Cotte et al.*, 1999; *Bao et al.*, 2015] to the east of the area focused on in our study. *Rapine et al.* [2003] observe the lowest group velocities at 33 s in dispersion measurements and find that a low-velocity layer in the midcrust is needed to explain the data in southern Tibet. They attribute this to the presence of melt. They argue that melting occurs due to $H_2O$ saturation and high crustal heat production resulting from a thickened crust in this region. *Caldwell et al.* [2009] also argue that the low-velocity layer they observe is due to partial melting in the upper crust in the presence of water.

In the Lhasa Terrane, the shear wave velocity reduction observed in the midcrust observed in this study is ~10%, from an average of 3.45 km/s to 3.12 km/s. Elevated temperatures are the simplest explanation for low-velocity layers [*Christensen*, 1979]. *McKenzie and Priestley* [2008] argue that crustal radioactivity in thickened crust is sufficient to cause midcrustal temperatures to increase, which would cause $V_s$ to decrease. Their model may contain melt at midcrustal depths, but melt is not required to explain the low midcrustal wave speeds.

The low-velocity layer is present in the models for all but two of the stations in the Lhasa Terrane (WT13 and WT05). The ubiquity of the low-velocity layer would also lend support to a thermal origin. From the data presented in this study it is not possible to draw a decisive conclusion regarding whether channel flow, that some argue for beneath Tibet and the Himalayas, is occurring here; however, the presence of the midcrustal low-velocity layer would be one observation that would be expected if it were occurring. The velocity models for stations 116, 177, and 118, just south of the ATF, also include a low-velocity layer in the midcrust. These stations are restricted to a limited geographical area and there are no other stations located nearby south of the ATF. It should be noted that Tertiary to Neogene basaltic volcanism has occurred in northwestern Tibet [*Arnaud et al.*, 1992], which may support the idea that melt is present beneath this part of the Plateau.

*Razi et al.* [2014] do not observe a low-velocity zone in the midcrust beneath stations in the Y2 array in their body wave tomography images and argue that there is a well-defined boundary north and south of the Karakoram Fault. The shear velocity models in our study are at odds with this: the low-velocity zone in the midcrust is observed to the north and south of the Karakoram Fault, suggesting that the fault does not act to separate two crustal regions. With the exception of the Altyn Tagh Fault, there is no indication from our velocity models that strike-slip faults in western Tibet cut through the entire crust. This is an observation that run counter to the idea that deformation in Tibet is primarily occurring along strike-slip faults bounding rigid blocks [*Molnar and Tapponnier*, 1975].

### 5.3. Lower Crustal Structure in the Lhasa Terrane

From H-$\kappa$ stacking and CCP stacks of *P* receiver functions along a transect $\sim$ 80°N, *Zhang et al.* [2014] observe evidence of conversions from a velocity contrast at a depth of 54–65 km beneath nearly all of the Lhasa block. Their Moho estimates in this region are at depths of 67.5–77 km. They interpret this as being the signal from the top of a partially eclogitized layer, where variations in amplitudes and delay times may be due to variations in the degree of eclogitization controlled by variations in the amount of water present in the crust. They suggest that eclogitization may be at an earlier stage in the Northern part of the Lhasa block than in the southern part. This is a feature similar to that seen farther east by *Acton et al.* [2011], *Nábělek et al.* [2009], *Schulte-Pelkum et al.* [2005], and *Kind et al.* [2002].

The velocity models, for some of the stations in the Lhasa Terrane in our study (MTH, HNL, SQAH, WT15, WT12, and WT06), do show some evidence of a small velocity increase at depths above where we pick the Moho. With the exception of WT17, ZMBA, and WT09, there is also clear evidence of a conversion in the receiver functions at delay times prior to the conversion that is likely to be from the Moho; however, most of the velocity models for these stations do not show evidence for a significant velocity increase above the Moho.

It may be that our velocity models are smoothed due to the inclusion of surface waves in the inversion and so do not resolve the velocity increase suggested by *Zhang et al.* [2014]. However, caution should also be exercised in overinterpreting receiver observations without using constraints from other methods. The interpretation made by *Zhang et al.* [2014] relies on results from H-$\kappa$ stacking, a method that in a region such as West Tibet may not give reliable results due to the effect of multiples from layers within the crust and the Moho boundary not being sharp.

## 6. Conclusions

Using velocity models resulting from the joint inversion of *P* receiver function and fundamental mode Rayleigh wave group velocity dispersion, we estimate Moho depth throughout the western part of the Indo-Eurasian collision zone. We bring together data from four different arrays, allowing for measurements to be made from the Indian Foreland Basin, across the Himalayas and Tibet and into the Tarim basin.

Across the Himalayas, Moho depths increase northward, with a $\sim$5 km jump at the Main Central Thrust. Moho depths agree well with those from studies farther east in the Himalayas. Beneath the Lhasa, Qiangang and Songpan-Ghanze Terranes in western Tibet, the Moho is at a depth of 68–86 km. The Moho depths are larger than those seen beneath the eastern side of the Plateau. No sharp change in Moho depth is observed crossing the boundaries between these terranes or at the Karakoram Fault. This is different to what is observed around 500 km to the east by *Nábělek et al.* [2009] who suggest that there is a boundary at 31°N and by *Zhang et al.* [2014] in this region, who argue that small changes in Moho depth provide evidence for whole-crustal shear zones in the Lhasa Terrane. In contrast, we do not see a significant step in the Moho until a large increase in Moho depth ($\sim$20–30 km) at the Altyn Tagh Fault at around 36.5°N. This implies that there are differences between eastern and western Tibet and may be evidence that in West Tibet, Indian lithosphere is present beneath all of the Plateau.

Several previous Moho estimates for Tibet have been made from Common Conversion Point receiver function stacks. This approach can result in incorrect migration of receiver function signals if the velocity model used in the migrations are incorrect. We consider the Moho depths estimated in the West Tibet study to be an improvement on those made from CCP stacks as jointly inverting receiver function and surface wave data allows for better constraints to be placed on the velocity structure.

A low-velocity zone is observed in the midcrust throughout the Lhasa Terrane in West Tibet. Midcrustal low-velocity zones are also observed in East Tibet. This low-velocity zone does not appear to be interrupted by the Karakoram Fault, which is at odds with the interpretation of *Razi et al.* [2014] that there is a major difference in the seismic properties to the north and south of the Karakoram Fault.

## References

Acton, C., K. Priestley, S. Mitra, and V. Gaur (2011), Crustal structure of the Darjeeling Sikkim Himalaya and southern Tibet, *Geophys. J. Int.*, *184*(2), 829–852.

Ammon, C. J., G. E. Randall, and G. Zandt (1990), On the nonuniqueness of receiver function inversions, *J. Geophys. Res.*, *95*(B10), 15,303–15,318, doi:10.1029/JB095iB10p15303.

Arnaud, N., P. Vidal, P. Tapponnier, P. Matte, and W. Deng (1992), The high $K_2O$ volcanism of Northwestern Tibet: Geochemistry and tectonic implications, *Earth Planet. Sci. Lett.*, *111*(2), 351–367.

Ashish, A. Padhi, S. S. Rai, and S. Gupta (2009), Seismological evidence for shallow crustal melt beneath the Garhwal High Himalaya, India: Implications for the Himalayan channel flow, *Geophys. J. Int.*, *177*(3), 1111–1120.

Bao, X., et al. (2015), Two crustal low-velocity channels beneath SE Tibet revealed by joint inversion of Rayleigh wave dispersion and receiver functions, *Earth Planet. Sci. Lett.*, *415*, 16–24.

Bensen, G. D., M. H. Ritzwoller, M. P. Barmin, A. L. Levshin, F. Lin, M. P. Moschetti, N. M. Shapiro, and Y. Yang (2007), Processing seismic ambient noise data to obtain reliable broadband surface wave dispersion measurements, *Geophys. J. Int.*, *169*(3), 1239–1260, doi:10.1111/j.1365-246X.2007.03374.x.

Brandon, C., and B. Romanowicz (1986), A no-lid zone in the central Chang-Thang platform of Tibet: Evidence from pure path phase velocity measurements of long period Rayleigh waves, *J. Geophys. Res.*, *91*(B6), 6547–6564.

Brown, L., W. Zhao, K. Nelson, M. Hauck, D. Alsdorf, A. Ross, M. Cogan, M. Clark, X. Liu, and J. Che (1996), Bright spots, structure, and magmatism in southern Tibet from INDEPTH seismic reflection profiling, *Science*, *274*(5293), 1688–1690.

Caldwell, W. B., S. L. Klemperer, S. S. Rai, and J. F. Lawrence (2009), Partial melt in the upper-middle crust of the northwest Himalaya revealed by Rayleigh wave dispersion, *Tectonophysics*, *477*(1), 58–65.

Caldwell, W. B., et al. (2013), Characterizing the Main Himalayan Thrust in the Garhwal Himalaya, India with receiver function CCP stacking, *Earth Planet. Sci. Lett.*, *367*, 15–27.

Christensen, N. I. (1979), Compressional wave velocities in rocks at high temperatures and pressures, critical thermal gradients, and crustal low-velocity zones, *J. Geophys. Res.*, *84*(B12), 6849–6857.

Cotte, N., H. Pedersen, M. Campillo, J. Mars, J. Ni, R. Kind, E. Sandvol, and W. Zhao (1999), Determination of the crustal structure in southern Tibet by dispersion and amplitude analysis of Rayleigh waves, *Geophys. J. Int.*, *138*(3), 809–819.

Dricker, I., and S. Roecker (2002), Lateral heterogeneity in the upper mantle beneath the Tibetan plateau and its surroundings from SS-S travel time residuals, *J. Geophys. Res.*, *107*(B11), 2305, doi:10.1029/2001JB000797.

Gilligan, A., S. W. Roecker, K. F. Priestley, and C. Nunn (2014), Shear velocity model for the Kyrgyz Tien Shan from joint inversion of receiver function and surface wave data, *Geophys. J. Int.*, *199*(1), 480–498.

Griot, D.-A., J.-P. Montagner, and P. Tapponnier (1998), Phase velocity structure from Rayleigh and Love waves in Tibet and its neighboring regions, *J. Geophys. Res.*, *103*(B9), 21,215–21,232.

Herrmann, R. B., and C. J. Ammon (2004), *Computer Programs in Seismology: Surface Waves, Receiver Functions and Crustal Structure*, Saint Louis Univ., St. Louis, Mo.

Houseman, G. A., D. P. McKenzie, and P. Molnar (1981), Convective instability of a thickened boundary layer and its relevance for the thermal evolution of continental convergent belts, *J. Geophys. Res.*, *86*(B7), 6115–6132.

Kennett, B. L. N., E. R. Engdahl, and R. Buland (1995), Constraints on seismic velocities in the Earth from traveltimes, *Geophys. J. Int.*, *122*(1), 108–124, doi:10.1111/j.1365-246X.1995.tb03540.x.

Kind, R., et al. (2002), Seismic images of crust and upper mantle beneath Tibet: Evidence for Eurasian plate subduction, *Science*, *298*(5596), 1219–1221.

Klemperer, S. L., B. M. Kennedy, S. R. Sastry, Y. Makovsky, T. Harinarayana, and M. L. Leech (2013), Mantle fluids in the Karakoram fault: Helium isotope evidence, *Earth Planet. Sci. Lett.*, *366*, 59–70.

Leech, M. L. (2008), Does the Karakoram fault interrupt mid-crustal channel flow in the western Himalaya?, *Earth Planet. Sci. Lett.*, *276*(3), 314–322.

Ligorria, J. P., and C. J. Ammon (1999), Iterative deconvolution and receiver-function estimation, *Bull. Seismol. Soc. Am.*, *89*(5), 1395–1400.

Mahesh, P., S. Gupta, S. Rai, and P. R. Sarma (2012), Fluid driven earthquakes in the Chamoli region, Garhwal Himalaya: Evidence from local earthquake tomography, *Geophys. J. Int.*, *191*(3), 1295–1304.

Mahesh, P., S. Rai, K. Sivaram, A. Paul, S. Gupta, R. Sarma, and V. Gaur (2013), One-dimensional reference velocity model and precise locations of earthquake hypocenters in the Kumaon–Garhwal Himalaya, *Bull. Seismol. Soc. Am.*, *103*(1), 328–339.

McKenzie, D., and K. Priestley (2008), The influence of lithospheric thickness variations on continental evolution, *Lithos*, *102*(1), 1–11.

Mitra, S., K. Priestley, V. Gaur, S. Rai, and J. Haines (2006), Variation of Rayleigh wave group velocity dispersion and seismic heterogeneity of the Indian crust and uppermost mantle, *Geophys. J. Int.*, *164*(1), 88–98.

Molnar, P. (1990), S-wave residuals from earthquakes in the Tibetan region and lateral variations in the upper mantle, *Earth Planet. Sci. Lett.*, *101*(1), 68–77.

Molnar, P., and P. Tapponnier (1975), Cenozoic tectonics of Asia: Effects of a continental collision, *Science*, *189*, 419–426.

Molnar, P., P. England, and J. Martinod (1993), Mantle dynamics, uplift of the Tibetan plateau, and the Indian monsoon, *Rev. Geophys.*, *31*(4), 357–396.

Nábělek, J., et al. (2009), Underplating in the Himalaya-Tibet collision zone revealed by the Hi-CLIMB experiment, *Science*, *325*(5946), 1371–1374.

Nelson, K. D., et al. (1996), Partially molten middle crust beneath southern Tibet: Synthesis of project INDEPTH results, *Science*, *274*(5293), 1684–1688.

Oreshin, S., S. Kiselev, L. Vinnik, K. Surya Prakasam, S. S. Rai, L. Makeyeva, and Y. Savvin (2008), Crust and mantle beneath western Himalaya, Ladakh and western Tibet from integrated seismic data, *Earth Planet. Sci. Lett.*, *271*(1-4), 75–87, doi:10.1016/j.epsl.2008.03.048.

Ozalaybey, S., M. K. Savage, A. F. Sheehan, J. N. Louie, and J. N. Brune (1997), Shear-wave velocity structure in the northern Basin and Range province from the combined analysis of receiver functions and surface waves, *Bull. Seismol. Soc. Am.*, *87*(1), 183–199.

Priestley, K., E. Debayle, D. McKenzie, and S. Pilidou (2006), Upper mantle structure of eastern Asia from multimode surface waveform tomography, *J. Geophys. Res.*, *111*, B10304, doi:10.1029/2005JB004082.

Rai, S., K. Priestley, V. Gaur, S. Mitra, M. Singh, and M. Searle (2006), Configuration of the Indian Moho beneath the NW Himalaya and Ladakh, *Geophys. Res. Lett.*, *33*, L15308, doi:10.1029/2006GL026076.

Rapine, R., F. Tilmann, M. West, J. Ni, and A. Rodgers (2003), Crustal structure of northern and southern Tibet from surface wave dispersion analysis, *J. Geophys. Res.*, *108*(B2), 2120, doi:10.1029/2001JB000445.

Razi, A. S., V. Levin, S. W. Roecker, and G.-c. D. Huang (2014), Crustal and uppermost mantle structure beneath western Tibet using seismic traveltime tomography, *Geochem. Geophys. Geosyst.*, *15*, 434–452, doi:10.1002/2013GC005143.

Schulte-Pelkum, V., and Y. Ben-Zion (2012), Apparent vertical moho offsets under continental strike-slip faults from lithology contrasts in the seismogenic crust, *Bull. Seismol. Soc. Am.*, *102*(6), 2757–2763.

Schulte-Pelkum, V., G. Monsalve, A. Sheehan, M. Pandey, S. Sapkota, R. Bilham, and F. Wu (2005), Imaging the Indian subcontinent beneath the Himalaya, *Nature*, *435*(7046), 1222–1225.

Searle, M., and R. Phillips (2008), Comment on: Does the Karakoram fault interrupt mid-crustal channel flow in the western Himalaya? by Mary L. Leech, *Earth Planet. Sci. Lett.*, *276*, 314–322.

Wei, W., et al. (2001), Detection of widespread fluids in the Tibetan crust by magnetotelluric studies, *Science*, *292*(5517), 716–719.

Wittlinger, G., J. Vergne, P. Tapponnier, V. Farra, G. Poupinet, M. Jiang, H. Su, G. Herquel, and A. Paul (2004), Teleseismic imaging of subducting lithosphere and Moho offsets beneath western Tibet, *Earth Planet. Sci. Lett.*, *221*(1-4), 117–130, doi:10.1016/S0012-821X(03)00723-4.

Yin, A., and T. M. Harrison (2000), Geologic evolution of the Himalayan-Tibetan orogen, *Annu. Rev. Earth Planet. Sci.*, *28*(1), 211–280.

Yuan, X., J. Ni, R. Kind, J. Mechie, and E. Sandvol (1997), Lithospheric and upper mantle structure of southern Tibet from a seismological passive source experiment, *J. Geophys. Res.*, *102*(B12), 27,491–27,500.

Zhang, Z., Y. Wang, G. A. Houseman, T. Xu, Z. Wu, X. Yuan, Y. Chen, X. Tian, Z. Bai, and J. Teng (2014), The Moho beneath western Tibet: Shear zones and eclogitization in the lower crust, *Earth Planet. Sci. Lett.*, *408*, 370–377.

Zhao, J., et al. (2010), The boundary between the Indian and Asian tectonic plates below Tibet, *Proc. Nat. Acad. Sci.*, *107*(25), 11,229–11,233, doi:10.1073/pnas.1001921107.

Zhao, W., and K. Nelson (1993), Deep seismic reflection evidence for continental underthrusting beneath southern Tibet, *Nature*, *366*(6455), 557–559.

Zhao, W., et al. (2001), Crustal structure of central Tibet as derived from project INDEPTH wide-angle seismic data, *Geophys. J. Int.*, *145*(2), 486–498.

Zhao, W., et al. (2011), Tibetan plate overriding the Asian plate in central and northern Tibet, *Nat. Geosci.*, *4*(12), 870–873.